Ophthalmic wavefront measurements using a versatile pyramid sensor

Elizabeth M. Daly* and Chris Dainty

Applied Optics Group, School of Physics, National University of Ireland Galway, University Road, Galway, Ireland

*Corresponding author: elizabeth.daly@nuigalway.ie

Received 26 January 2010; revised 14 June 2010; accepted 19 June 2010; posted 21 June 2010 (Doc. ID 123318); published 15 July 2010

We describe the operation of a pyramid wavefront sensor used to measure and correct aberrations of the human eye. The system is designed for maximum speed when running in closed loop but can also provide calibrated open-loop measurements of aberrations with a range of sampling options. A detailed characterization of the system was performed to ensure measurement accuracy. Ocular aberrations after correction had root-mean-square errors consistently less than 0.1 μm over a 6 mm pupil for all subjects tested. The system frame rate is 83 Hz in both open- and closed-loop modes. © 2010 Optical Society of America

OCIS codes: 010.7350, 010.1080, 330.4460.

1. Introduction

Adaptive optics (AO) systems for living human eyes [1–3] have traditionally been based upon the well-known Shack–Hartmann sensor [4,5] to provide measurements of the wavefront slopes, which are then used as feedback to the AO control loop. At about the same time as the first ophthalmic implementation of AO [1], a new type of sensor, the pyramid wavefront sensor (PWS), was proposed and demonstrated for astronomical applications [6,7]. The pyramid wavefront sensor is based upon the Foucault knife-edge test [8] but uses a refractive element (four-faceted pyramid) in the focal plane to divide the wavefront into four parts, each going on to form a conjugate image of the entrance pupil at the wavefront sensing camera. With appropriate orientation of the pyramid, this arrangement is equivalent to two knife edges in the orthogonal x and y directions. The intensity distribution among the four pupil images is then proportional to the local x and y wavefront slopes. The sensor range is usually extended by introducing some type of dynamic modulation, of either the pyramid itself or the focused beam, although alternatives have been proposed or implemented [9–12]. The pyramid sensor has been used to successfully measure [11] and correct [13] ocular aberrations *in vivo*. There are many apparent practical advantages to using the pyramid wavefront sensor rather than the traditional Shack–Hartmann one. Chief among these is the fact that the sensor gain or response (measured sensor signal versus input wavefront slope) can be easily adjusted experimentally, as can the sampling of the slopes in the pupil plane. This is in contrast with the equivalent adjustment for a Shack–Hartmann sensor, which would require physically changing the lenslet array focal length and/or the use of a zoom lens to modify pupil sampling. Simulations have also shown that the pyramid sensor should provide better sensitivity than the Shack–Hartmann sensor when used in a closed-loop AO system [14,15]. Finally, there is some evidence that the pyramid sensor may be more robust to speckle noise than the Shack–Hartmann sensor when a laser is used as the probing source [13]. Shack–Hartmann sensors must employ some method to average out the speckle caused by the roughness of the retina, and those adaptations do not appear to be necessary with the pyramid sensor.

0003-6935/10/310G67-11$15.00/0

A previous study [13] has demonstrated that the PWS can be used in ophthalmic AO. The aim of this paper is to clearly present the choices that must be made when designing such a system for optimum performance. The implications of those choices are considered. The opposing requirements of open- (accurate measurement of possibly large aberrations) and closed- (highly sensitive measurement of reduced aberrations) loop *in vivo* operation are discussed in detail. In Section 2, our system is described in detail and the relationship between measured quantities and experimental variables is clarified. Section 3 describes a detailed calibration and verification of the setup. *In vivo* results are presented and discussed in Section 4.

2. System Description

A schematic of the apparatus is shown in Fig. 1. The system is designed to measure and correct ocular aberrations over a 6 mm pupil at 675 nm. To avoid corneal reflections, the narrow probe beam (diameter <1 mm) enters the eye off axis and via two mirrors placed in conjugate retinal and pupil planes, which allow independent control of the probe position and incident angle, respectively, at the eye. The path for wavefront sensing passes lenses 1 to 8 to the CCD (Retiga EXi, Qimaging, Burnaby, BC, Canada) where the reimaged ocular pupil diameter is $\sim$600 μm. Each reimaged pupil contains 96, 48, 24, or 12 samples across the diameter, depending on CCD pixel binning (B1, B2, B4, and B8 refer to CCD pixel binning of 1×1, 2×2, 4×4, and 8×8 pixels, respectively). The coarsest spatial sampling option is matched to the minimum required to perform AO with the chosen deformable mirror (DM). The sensing light is focused at the vertex of a glass pyramid (custom made with vertex angle 178 deg, diameter 9 mm), where the F number is $\sim$33. This F number avoids overlap of the four exiting beams, while ensuring the best data-packing configuration of the reimaged pupils on the CCD for this particular pyramid [16]. The aberration-free point spread function at the pyramid tip is 27 μm (distance between the peak and first zero), calculated at the sensing wavelength of 675 nm. The raw sensor signals Sx and Sy at each point in the pupil can be determined from the relative intensities in the corresponding points of the conjugate pupil images at the CCD:

$$Sx(x,y)=\frac{[I_1(x,y)+I_3(x,y)]-[I_2(x,y)+I_4(x,y)]}{\sum_{i=1}^{4}I_i(x,y)},$$
$$Sy(x,y)=\frac{[I_1(x,y)+I_2(x,y)]-[I_3(x,y)+I_4(x,y)]}{\sum_{i=1}^{4}I_i(x,y)}, \quad (1)$$

where $I_i(x,y)$ is the intensity at point (x,y) in pupil i and the pupils at the CCD are numbered according to Fig. 1. Because of normalization by the total intensity, these raw sensor signals can take on values in the range $[-1,+1]$, although a value of ±1 implies saturation of the sensor. For small aberrations, these normalized intensity differences are proportional to the x and y slopes of the wavefront in the pupil. The proportionality constant is set here by introducing a dynamic modulation of the focused beam using a steering mirror (FSM-300, Newport, Irvine, California, USA) placed in a conjugate pupil plane. This element drives the focused beam in a circular path (100 Hz) around the vertex of the pyramid. In the geometrical optics regime, the local wavefront slopes are found by applying the appropriate scaling to the raw sensor signals above:

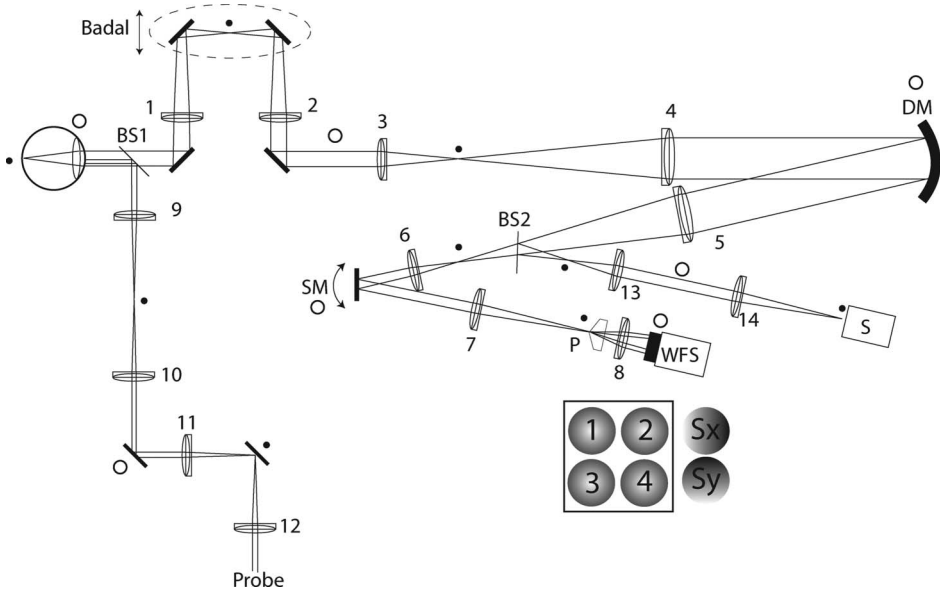

Fig. 1. Schematic optical setup showing probe, wavefront sensing (WFS), and science arms: BS1 and BS2, pellicle beam splitters; 1–14, lenses; DM, deformable mirror; SM, steering mirror; WFS, wavefront sensing camera; S, science camera. Retinal plane and conjugates are marked with dots, pupil plane and conjugates with open circles. Sx and Sy are the unscaled x and y gradients obtained from the pupils 1 to 4.

$$\frac{\partial W(x,y)}{\partial x} = \frac{R_{\mathrm{mod}}}{f}\sin\left[\frac{\pi}{2}Sx(x,y)\right] \approx \frac{R_{\mathrm{mod}}}{f}\left[\frac{\pi}{2}Sx(x,y)\right], \qquad \frac{\partial W(x,y)}{\partial y} = \frac{R_{\mathrm{mod}}}{f}\sin\left[\frac{\pi}{2}Sy(x,y)\right] \approx \frac{R_{\mathrm{mod}}}{f}\left[\frac{\pi}{2}Sy(x,y)\right]. \tag{2}$$

Here, R_{mod} is the radius of dynamic modulation at the pyramid vertex, f (100 mm) is the focal length of lens 7 in Fig. 1, and the assumption is that Sx and Sy are both small. These equations are valid so long as $|\partial W/\partial x|$ and $|\partial W/\partial y|$ are $\ll R_{\mathrm{mod}}/f$, and an analysis of sensor linearity has shown that this simple geometrical analysis, rather than a more detailed one based on diffraction theory, is perfectly sufficient [17]. From Eq. (2), it is clear that the sensor sensitivity (ratio of Sx to $|\partial W/\partial x|$) is inversely proportional to the modulation angle R_{mod}/f. It is possible to adjust R_{mod} by controlling the voltage applied to the steering mirror. In this work, we use a range of voltage settings, which provide R_{mod} values equivalent to 2.7, 4.5, 9.1, 13.6, and 18.2 times the aberration-free point spread function (distance between the peak and first zero). Here, these modulation settings are referred to for simplicity as M3, M5, M10, M15, and M20, respectively. The modulation can also be expressed as multiples of a unitary tilt angle λ/D [14], where λ is the sensing wavelength (675 nm) and D is the diameter of the conjugate pupil image at the steering mirror (3 mm). Table 1 shows the modulation settings expressed in multiples of the aberration-free point spread function and in multiples of the unitary tilt angle λ/D.

Two mirrors located between lenses 1 and 2 form a Badal stage to compensate for the subject's defocus ($\pm 2D$), while the DM (19-actuator piezoelectric device from Flexible Optical BV, Delft, The Netherlands) placed in a conjugate pupil plane is used to correct higher-order ocular aberrations. The footprint of the beam at this location is 18 mm, or 60% of the manufacturer's active diameter. This choice is based on a previous study of DM performance [18], where typical ocular wavefronts were generated using the statistical model of Thibos *et al.* [19] and fitted in simulation using different amounts of the mirror diameter. That study predicted the best performance from this mirror when using 64% of the mirror diameter, allowing placement of a ring of actuators, and therefore providing large correction ability, at the pupil edge. In simulation, we found that the residual RMS error on using this mirror to correct a typical set of eyes, generated with the Thibos model, is reduced by 16% when using 60% rather than 100% of the DM diameter. A fraction (~8%) of the corrected beam is picked of by a beam splitter (BS2 in Fig. 1) and directed to a camera (Luca EM 247, Andor Technology PLC, Belfast, U.K.), where a retinal conjugate is formed by lenses 13 and 14. This allows us to record the ocular double-pass point spread function for verification of the correction provided by the AO system. Not shown in the schematic are two calibration arms, which deliver collimated reference flats for open- and closed-loop operation.

Table 1. Radius of the Modulated Circular Path at the Pyramid Vertex in Multiples of the Aberration-Free Point Spread Function[a] with Corresponding Tilt Values[b]

Modulation Setting	× PSF	$\times\lambda/D$
M3	2.7	3.3
M5	4.5	5.5
M10	9.1	11.1
M15	13.6	16.6
M20	18.2	22.2

[a]PSF, peak to first zero.
[b]In multiples of a unitary tilt angle λ/D.

A. Interface

A custom LabVIEW (National Instruments, Austin, Texas, USA) interface controls the experiment. It allows setting of all basic experimental parameters, identification and correct ordering of the pupils for slope calculations, and open- and closed-loop control of the system. Closed-loop control is based on the standard least-squares controller, the calculated correction being applied iteratively via a loop gain. A feature of our system is that the loop gain can be fixed (default) or variable depending on the value of a metric; we use the RMS of the corrected wavefront after correction. For aberrations that are not changing very quickly, lowering the loop gain can result in more stable operation of the system. Calculation of this metric requires live wavefront reconstruction, and we can display the individual Zernike terms to allow, for example, optimization of the Badal setting for a particular subject. The speed of the system running in open and closed loop (with and without wavefront reconstruction), as a function of CCD binning, is shown in Fig. 2. Obviously, there is a trade-off between speed and spatial resolution of the measured gradients. For closed-loop correction of ocular wavefronts, we typically use the fastest

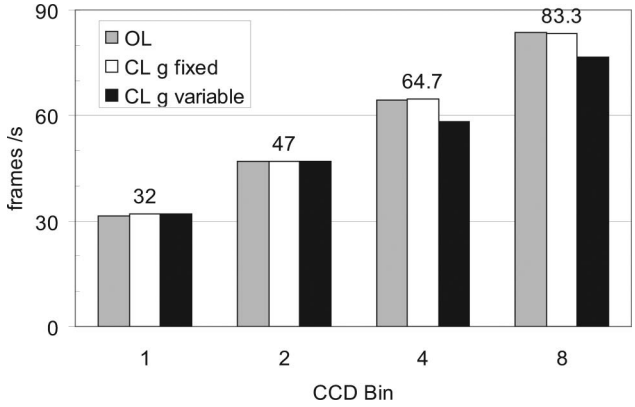

Fig. 2. System speed as a function of CCD pixel binning.

option, B8, which provides 12 samples of the gradient across the pupil. There is a reduction in speed for closed-loop operation with variable versus fixed gain [76 versus 83 frames per second (fps)] because the former requires extra time for wavefront reconstruction. The speeds shown in Fig. 2 include writing of gradient data to a file for off-line processing. In closed-loop mode, the required correction and DM control values are also stored at each iteration of the loop. Data to be stored are placed in a queue and passed to a parallel loop in LabVIEW, which can run on the machine's second processor. This parallel loop looks after file writing only and, because it runs in parallel with the main AO loop, it does not affect system speed. In this work, the maximum speed was limited by CCD readout of the chosen region of interest. In principle, there is nothing to prevent a reduction in exposure time (matched by an increase in the steering mirror drive frequency), compensated for by an increase in probe power.

3. System Verification

Data from the sensor were stored and processed off line to reconstruct the ocular wavefront by fitting the slopes to Zernike polynomials, to radial order $n = 7$, using a least-squares reconstructor. The accuracy of this process was established by comparing the results obtained in various tests to independent measurements of the phase obtained using a commercial digital interferometer (μPhase HR, FISBA OPTIK AG, St. Gallen, Switzerland). These comparisons were made at all combinations of CCD binning and steering mirror modulation, although in practice the lowest modulation setting results in such a limited linear sensor range that it is rarely used to measure ocular wavefronts.

A. Wavefront Reconstruction Error

The wavefront reconstruction error was estimated by inserting aberrations into the system using the DM, controlled by applying commands C in the range $[-1, +1]$, where $-1/+1$ corresponds to minimum/maximum applied voltage and $C = 0$ is the bias position. Biasing the DM means that half of the maximum voltage is applied to all actuators, ensuring the same amount of available positive and negative stroke. For $C = \pm 0.2$ applied to the central DM actuator, the resulting wavefront RMS error was approximately 0.130 μm, about the size of the residual error we expect when performing closed-loop AO on the eye. At each setting of CCD binning and steering mirror modulation, 30 frames of unscaled pyramid sensor signals were stored and the wavefront was reconstructed by fitting to Zernike polynomials. This gave an estimate of the phase, which we refer to as ψ_{pws}. We also measured the influence function matrix of the DM (IF_{int}) with the commercial interferometer—this contains the phase map obtained on poking each actuator. Using this information, we could calculate the phase resulting from application of $C = \pm 0.2$ to the central DM actuator, ψ_{int}, and compare the result to the pyramid sensor measurements. The RMS reconstruction error σ_{rec} was then given by the difference between the two phase estimates:

$$\sigma_{\mathrm{rec}} = \left[\sum_j [\psi_{\mathrm{int}}(j) - \psi_{\mathrm{pws}}(j)]^2\right]^{1/2}, \qquad (3)$$

where the index j refers to each sample in the pupil. The results obtained are shown in Fig. 3(a) and follow trends observed in [20]. We found that the reconstruction error varies from 0.025 to 0.050 μm. Regardless of the spatial sampling (CCD binning) used, there appears to be an optimum steering mirror modulation (not necessarily the smallest) that will minimize the reconstruction error. The error tends to increase slightly at the very lowest and highest modulation settings. Note that the error bars on the data are larger in general at higher modulations, reflecting the reduced sensitivity at these settings; a fixed

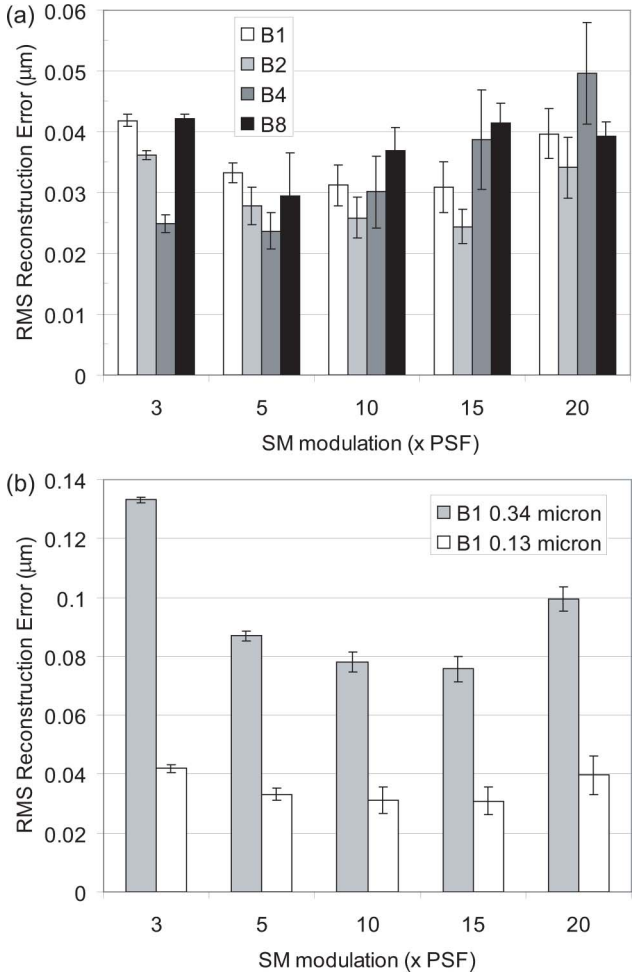

Fig. 3. (a) Experimental wavefront reconstruction error as a function of steering mirror modulation and CCD pixel binning. The applied wavefront has an RMS error of 0.13 μm. (b) Variation of the wavefront reconstruction error for B1 as a function of steering mirror modulation for two different applied wavefronts. Error bars are ± 1 standard deviation obtained from the 30 wavefront sensor frames.

wavefront gradient occupies a smaller fraction of the available $[-1,+1]$ sensor range, when R_{mod} is large, than it does when R_{mod} is small. For closed-loop AO, we typically use B8 and steering mirror modulation of M5 (B8M5), giving an estimated reconstruction error of about 0.030 μm. The resolution of this DM is limited by its 19 channels, so there is no advantage to increasing the sampling of the wavefront for closed-loop operation, but there would be a speed penalty to be paid. We repeated this test with a larger applied wavefront RMS error (0.340 μm or 3.2 rad), again induced using the central DM actuator, and found similar but more pronounced trends; see Fig. 3(b). Now the reconstruction error shows a significant increase for our lowest steering mirror modulation setting. This result is predicted for large input RMS errors (>1.5 rad), and comes from nonlinearities in the expressions relating pyramid sensor signal and phase in the diffractive optics regime [15]. Even our lower test wavefront, with RMS error of 0.130 μm (1.2 rad) was just below this threshold; hence, we do see a slight increase in the reconstruction error at M3 versus M5 modulation settings. This test was performed using the same exposure times (10 ms) and light levels as the *in vivo* measurements that will be described in Section 4. The average light intensity in a pupil image was always ≥45/255 analog-to-digital units (ADU), resulting in a signal to noise ratio of 34 dB for the CCD and ensuring photon-noise limited operation (8 e^- readout noise, 18,000 e^-/pixel full-well capacity). The effect of discretization noise alone ($\pm$1 bit in 8 bit data) was found to be insignificant compared to the experimentally determined values of Fig. 3, contributing ≤1 nm to the overall wavefront reconstruction error.

What is the expected reconstruction error? We followed the procedure outlined in [20,21] to calculate the noise propagation coefficients, n_k^2, from experimentally measured quantities: the two influence function matrices IF_{int} (relating phase maps to DM pokes) and IF_{pws} (relating pyramid sensor signals to DM pokes) and D, the matrix of Zernike derivatives used in reconstruction. These coefficients describe how noise propagates through the system from the raw sensor signals to noise on the fitted Zernike modes for a particular steering mirror modulation and CCD binning combination. They give the ratio of the variance of the kth mode in a Zernike decomposition of the wavefront to the sensor signal variance, $n_k^2 = \sigma_k^2/\sigma_s^2$. An estimate for the theoretical reconstruction error is found by summing the modal variances, σ_k^2, over the K modes used:

$$\sigma_{\mathrm{th}}^2 = \sum_k^K \sigma_k^2 = \sum_k^K \sigma_s^2 n_k^2 = \frac{1}{N}\sum_k^K n_k^2, \tag{4}$$

where we assume, for simplicity, that σ_s^2 varies only with the number of incident photons N. We confirmed this in experiment by varying the average light intensity in the pupil images and calculating the variances of the resulting raw sensor signals on application of a reference wavefront. We found that the variance on the raw signals decreased steadily, and followed a power law, as the number of ADU in the pupil image was increased by known increments. There was negligible change in the raw sensor signal variances on varying CCD binning or steering mirror modulation. If the noises of all measurements are independent and have the same variance [22], then the coefficients n_k^2 are the diagonal elements of the matrix product G^TG, where G is given by

$$G = (IF_{\mathrm{int}})(IF_{\mathrm{pws}})^T D^T. \tag{5}$$

.

There is a unique matrix G for each combination of steering mirror modulation and CCD binning. For example, if N is in the range 10–1000 photons/m^2 and the steering mirror modulation is M5, then at B8 this calculation yields σ_{th} in the range 0.300–0.030 μm, the lowest value just agreeing with our experimental estimate of Fig. 3. Using B1, the expected error σ_{th} reduces to 0.070–0.007 μm, which is in better agreement with our experimental value. If photon number and CCD binning are held constant, this analysis predicts that the reconstruction error should increase with steering mirror modulation (the matrix IF_{pws} is sensitive to this setting), and we do observe that trend in Fig. 3 once the optimum steering mirror modulation is exceeded. We conclude that our estimates for wavefront reconstruction error are sensible and within the expected range. Finally, using ophthalmic trial lenses to produce defocus and astigmatism, we confirmed that the sensor linear range increased as modulation was increased.

B. Dynamic Behavior

Our AO system operates in the standard closed-loop configuration: the correcting device is placed before the wavefront sensor and the error signal for the control loop is the residual RMS error of the wavefront after correction. The integral controller allows calculation of the DM commands for the next loop iteration, C_{i+1} (a vector with 19 elements), through

$$C_{i+1} = -gC_i(SXY_i - SXY_{\mathrm{CLref}}) + C_i, \tag{6}$$

where g is the loop gain (range 0–1), SXY_{CLref} is a reference signal corresponding to a flat wavefront introduced immediately after the DM, and C_i and SXY_i are the DM command vector and the measured sensor signals at the previous loop iteration. We typically use $g = 0.5$ for ocular measurements as it seems to be a good compromise between loop stability and correction ability. The temporal behavior of the system can be simply modeled using Laplace Transforms for four components [23]:

- $G_{\mathrm{WFS}}(s)$: The wavefront sensor (WFS) behaves as a simple integrator over the exposure time T;

- $G_D(s)$: Delay, τ, due to CCD readout and slope calculation;
- $G_C(s)$: Simple integration control of the loop based on the system frame rate $1/T_f$, where $T_f = T + \tau$;
- $G_H(s)$: DM commands held constant for duration of each frame T_f.

Here, we assume that the DM itself does not contribute any delay; this is true for our system, as we could measure no difference in the frame rates of the system running in open loop (no DM control) versus closed loop (active DM control). The open-loop transfer function, $G_{\mathrm{OL}}(s)$, is given by the product of the four terms above:

$$G_{\mathrm{OL}}(s) = \left(\frac{1 - e^{-Ts}}{Ts}\right)(e^{-\tau s})\left(\frac{g}{1 - e^{-T_f s}}\right)\left(\frac{1 - e^{-T_f s}}{T_f s}\right). \tag{7}$$

From this, we confirmed the stability of the system: positive gain and phase margins for all values of g and system frame rate (pixel binning). An estimate of the theoretical system bandwidth was obtained by measuring the frequency at which $G_{\mathrm{OL}}(s)$ crosses 0 dB. This is a function of the frame rate and loop gain. For example, at B8 and $g = 0.5$, the open-loop bandwidth is calculated to be ~9 Hz with gain margin 16 dB and phase margin 76 deg.

To evaluate closed-loop performance, we look at the closed-loop and error transfer functions:

$$G_{\mathrm{CL}}(s) = \left(\frac{G_{\mathrm{OL}}(s)}{1 + G_{\mathrm{OL}}(s)}\right), \tag{8}$$

$$E(s) = \left(\frac{1}{1 + G_{\mathrm{OL}}(s)}\right). \tag{9}$$

A common way to quantify closed-loop performance is to plot the error transfer function $E(s)$ and to identify the maximum frequency where this quantity is ≤0 dB. This is equivalent to finding the maximum frequency where the ratio $G_{\mathrm{CL}}(s)/G_{\mathrm{OL}}(s)$ is less than unity. At B8 and $g = 0.5$, we estimate the theoretical closed-loop bandwidth or our system to be ~9 Hz. Figure 4 summarizes some of these results.

1. *Loop Closure Speed and Accuracy*

We examined the time taken to close the loop on a static aberration of magnitude 0.340 μm RMS (described in Subsection 3.A) as a function of loop gain. We estimated this as the time required for the RMS error to reduce to a stable value—see Fig. 5. Gain values $g \le 0.7$ provided stable operation, although a small oscillation creeps into the final RMS error once the gain goes above 0.5. For $g = 0.8$, the loop does remain closed, but the corrected RMS error rises to about half of the open-loop value after ~0.5 s. We find that the time taken to close the loop reaches a steady state once the gain is greater than 0.3. We can estimate the closed-loop bandwidth or our AO system as the inverse of this time—approximately 6 Hz. We also checked the residual RMS error on correcting this static aberration with fixed loop gain ($g = 0.5$), but as a function of CCD pixel binning and steering

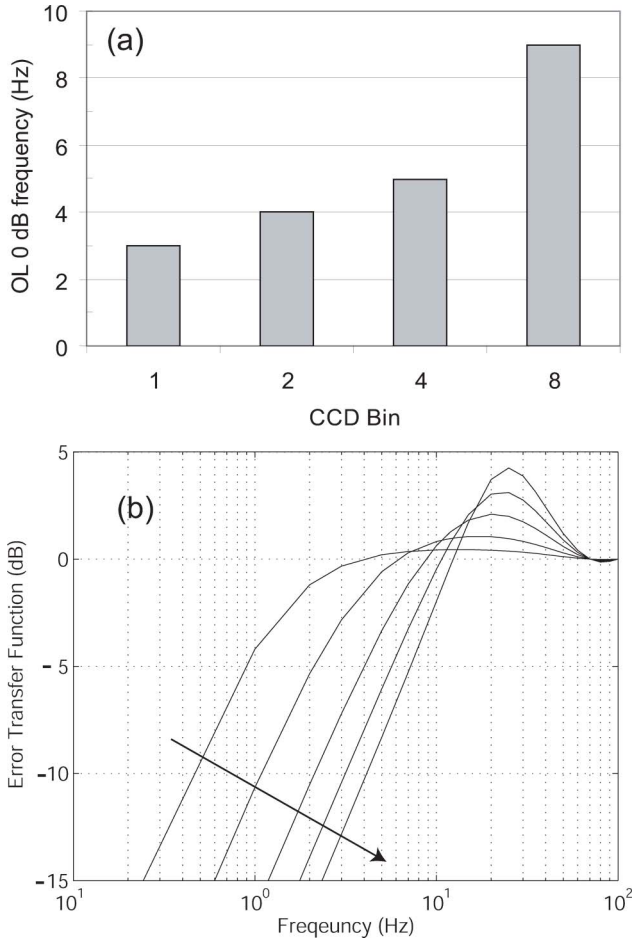

Fig. 4. (a) Predicted open-loop bandwidth obtained from the simple model. (b) Modeled error transfer function with loop gain g increasing in the direction of the arrow, taking values [0.1, 0.25, 0.5, 0.75, 1].

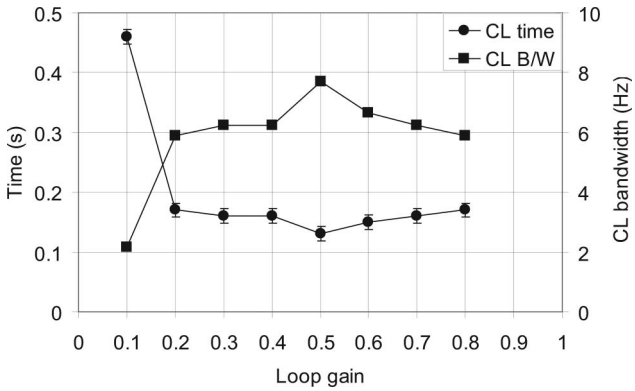

Fig. 5. Time taken to reduce the RMS error to a stable closed-loop value on applying a static aberration (0.340 μm RMS) at B8M5, $g = 0.5$. Filled circles are experimental data points, with error bars given by the sampling accuracy (±0.012 s at 83 fps). Filled squares are estimates for bandwidth using the inverse of the time values.

mirror modulation. We found that the quality of correction deteriorated as steering mirror modulation was increased and the effect was more pronounced for coarse (B8) rather than fine (B1) sampling; the residual RMS error after loop closure rose from 0.013 to 0.040 μm at B1, and from 0.027 to almost 0.200 μm at B8, as the modulation was increased from M5 to M20. This is to be expected from a consideration of pyramid sensor sensitivity (ratio of measured sensor signal to aberrations in the incident wavefront), which is inversely proportional to the modulation angle. When the loop is partially closed, the incident aberrations reduce and the sensor signal reduces and occupies a smaller fraction of the available range $[-1, +1]$—the loop becomes less sensitive to small changes in the sensor signal. Ideally, the steering mirror modulation could be dynamically reduced in closed loop to maintain sensitivity as the sensor signals approach zero (flat wavefront). If, as in our setup, the steering mirror modulation is a fixed quantity during each measurement, then closed-loop operation with high modulation settings will exhibit low sensitivity and, thus, poorer loop performance.

C. Prediction of Closed-Loop Performance

At the second stage of verification, artificial phase plates [24] were placed in the pupil plane and a collimated beam was passed through them, allowing for open- or closed-loop testing. We confirmed that the system correctly identified the Zernike modes and their signs from plates exhibiting some pure terms —we use the OSA standard for reporting ocular aberrations where each mode is referred to by a single index J [25]. The phase plates were also measured with a commercial interferometer, and we confirmed that the results obtained agreed with open-loop pyramid sensor measurements. Closed-loop performance was modeled by fitting the phase-plate aberrations with the influence functions of the 19-actuator DM (contained in IF_{int}). This simulation predicted the DM commands required to provide static correction for each phase plate and the residual RMS error after fitting in each case. We then performed the experiment and compared the results to those predicted by the simulation. An example is shown in Fig. 6. This particular phase plate had aberrations similar to a typical eye (total RMS error of 0.98 μm), the major contributing terms being defocus (J4), astigmatism (J3 and J5), one coma term (J7), and spherical aberration (J12). On closing the loop, the RMS error drops from its initial high value to $\sim$0.074 μm, while the model predicts a residual RMS error of $\sim$0.1 μm. A map of the initial phase is shown in the inset to Fig. 6(a). Figure 6(b) compares the actual DM commands on loop closure with those predicted by the model for this plate. The data sets show the same trends; for example, actuators 1–7 generally all push in the same direction as expected for a defocus term; however, this term is not centered in the measurement pupil, and so actuators 2 and 3 deviate from that trend. The outer ring of actuators (8–19) also reflect this lack of symmetry, but the situation is complicated by the fact that they lie outside of the optical pupil. For this experiment, the Badal was not used so the DM was allowed to correct all aberrations including tip, tilt, and defocus. The same experiment performed on a phase plate exhibiting almost pure coma (J8) produced good correction (0.7 μm initial, 0.046 μm final, 0.058 μm predicted RMS), but a plate exhibiting trefoil (J9) could not be corrected as well in simulation or experiment (0.54 μm initial, 0.16 μm final, 0.15 μm predicted RMS). The reason for this is probably the limited spatial resolution of our DM rather than a problem of actuator stroke. The results presented here represent best-case correction expectation for real eye measurements, which have dynamic aberrations and are affected by blinks and other instabilities.

4. *In Vivo* Measurements

A. Protocol

The right eyes of eight subjects were studied—all subjects were healthy volunteers aged from 26 to

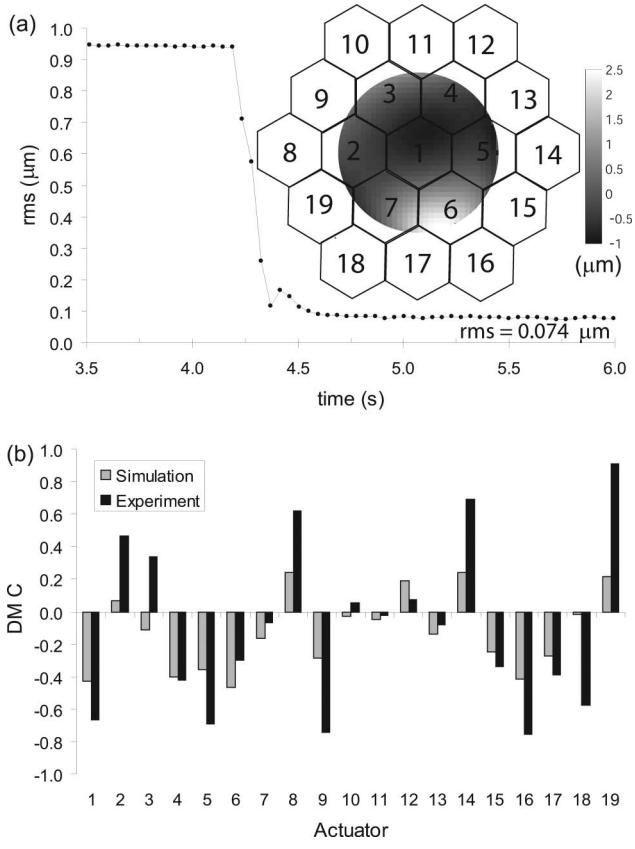

Fig. 6. (a) Experimental trace showing reduction of the RMS error on closing the loop on an artificial phase plate. Loop gain was $g = 0.5$ and steering mirror modulation = M5. Because this was a static aberration, there was no need for speed; therefore, CCD binning was B1 for maximum spatial resolution. The inset shows the initial phase map overlaid with a map of the DM showing actuator placement. (b) Comparison of actual DM commands after correction with those predicted by our model.

31 years. All subjects were dilated using 1% Tropicamide. This work has received ethical approval from the National University of Ireland Galway Research Ethics Committee. Each subject was stabilized using a bite bar and aligned to the system using a camera inserted in the conjugate pupil plane located between lenses 13 and 14 of Fig. 1. The retinal reflection of the incident probe beam provided enough light for this task, eliminating the need for a dedicated pupil illumination source. Probe beam power was typically 1–2 μW at the eye, well below the maximum permissible exposure level calculated for this wavelength (675 nm) [26]. For fixation, the subject looked at the laser beam, and the camera exposure time was 10 ms in all cases. Each measurement run lasted approximately 10 s, and three runs were stored at each setting to allow for averaging. All displays and diagnostics were switched off to achieve the maximum system speed.

B. Open-Loop Measurements

The challenge with the pyramid wavefront sensor is to ensure that sufficient dynamic range is available to accurately measure a given aberration. For ocular aberrations, this is completely subject specific, and the initial intention in this study was to identify that optimum steering mirror modulation for each subject. Starting at M5, a few seconds of sensor data (with no open-loop reference subtracted) were stored and processed off-line to check if the raw sensor signals were close to the limits of ± 1. If they were, the modulation was increased and the process repeated until either the maximum modulation was reached or it was clear that the raw signals were well within the linear range of the sensor. However, on doing this for the first subject, it became clear that the process was too time consuming. A decision was made to be conservative and use the largest steering mirror modulation setting (M20) for open-loop measurements of all subjects. We are conscious that this may not be the optimum for every subject, but it did allow direct comparisons among them. CCD binning was B8 to achieve the maximum sampling rate of 83 fps. These experimental conditions are hereafter referred to as B8M20. Under these conditions, from Fig. 3, we estimate the reconstruction error to be $\sim$0.100 μm. Note that, in open loop, we expect to measure larger aberrations than in closed loop, so we assume the reconstruction error to be closer to the value shown in part (b), rather than part (a), of Fig. 3. Before any data were stored, live wavefront reconstruction was activated allowing monitoring of the Zernike terms. The x and y tilts were then minimized through probe adjustment because we did not want these low-order terms to saturate the sensor. The Badal was left in the zero position (subject defocus was not compensated) and the DM was biased (all actuator commands $C = 0$) for all open-loop studies. Measurements of open-loop ocular aberrations were always referenced to a flat wavefront injected at the measurement pupil. Figure 7 shows the total wavefront RMS error for each subject with x and y tilts removed (J1 = J2 = 0 in the OSA standard). Subject 9 is the average of all subjects.

Although it was not practical to perform measurements on all subjects at all the different combinations of spatial sampling and steering mirror modulation, some extra work was done on a few subjects, allowing us to draw some general conclusions. For example, in a normal population of healthy eyes, the coefficient for spherical aberration (J12 in the OSA standard) is biased towards positive values [27]. At B8M20, the J12 coefficient was $\sim$0 for subject 1, although increasing the sampling to B4 at M20 allowed us to correctly identify this subject's negative J12. In general, we noticed that using B8 (12 samples across pupil diameter) rather than B4 (24 samples across pupil diameter) tended to overestimate the low-order Zernike terms (J = 3 – 5) at the expense of higher-order ones. Finally, if the spatial sampling of the pupil was kept constant but the steering mirror modulation was changed, we were able to confirm that the sensor saturated for some subjects. We observed this as a progressive reduction in the measured RMS of the wavefront as the modulation was decreased (observed for subjects 1, 4, and 5). The same was not true of subject 6 who has had laser eye surgery (photorefractive keratectomy); that subject's total RMS error remained constant through the steering mirror modulation settings M20 down to M5, indicating that the aberrations were indeed small enough to be measured accurately even on the smallest sensor range.

C. Closed-Loop Measurements

All closed-loop data were stored at B8 (for speed) and M5; initial investigations indicated that this modulation setting provided stable closed-loop correction for most subjects. At this setting, we assume the

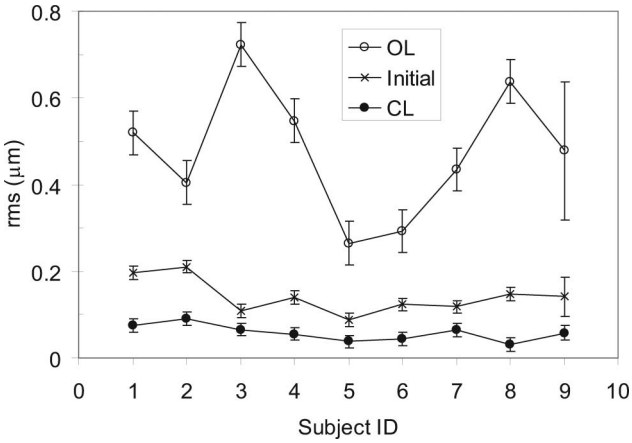

Fig. 7. RMS values for the eight subjects measured in open loop at B8M20 (open circles) and closed loop at B8M5 (filled circles). Also included are the initial RMS values at B8M5 before the loop was closed (crosses). Error bars are 0.100 μm long for open-loop data and 0.030 μm long for closed-loop and initial data. Subject 9 is the average subject with error bars in each series given by $\pm$ one standard deviation of the eight samples.

reconstruction error to be 0.030 μm—see Fig. 3(a). Closed-loop measurements were always referenced to a flat wavefront injected into the system immediately after the DM. Before any data were stored, live wavefront reconstruction was activated, allowing monitoring of the Zernike terms. The DM was biased, the Badal stage was used to minimize the subject's defocus (J4), and the x and y tilts were then minimized through probe adjustment. Two seconds of data were stored before the loop was closed and about 10 s afterward. The closed-loop RMS was calculated as the average of all the stable closed-loop data points after blinks were removed. The system provided good correction for all eight subjects—the average corrected RMS was 0.064 μm, although correction to almost 0.03 μm was achieved for subjects 5 and 8, which was essentially just the reconstruction error. The results are shown in Fig. 7. Note that the open-loop measurements at B8M20 were much larger than the initial RMS values measured at B8M5 prior to loop closure. There are several reasons for this. First, the true open-loop measurements were referenced to a flat wavefront injected into the system at the entrance pupil, while the initial and closed-loop measurements were referenced to a flat wavefront injected after the DM. Second, the Badal stage was not used to compensate for subject defocus in open loop (these RMS values include defocus), while in closed loop it was (defocus minimized)—a necessary step to avoid clipping of DM actuators. For example, the aberrations of subject 3 were dominated by defocus, and a lot of this was eliminated with the Badal stage alone. Third, although every effort was made to minimize x and y tilts before all scans, they were not always completely eliminated. However, the most important reason for the difference between the true open-loop measurement and the initial value before loop closure is that the sensor simply does not have enough measurement range at M5 to capture large gradients without saturation for all subjects. Note that the maximum value of the initial RMS errors before the loop was closed in this figure does not exceed 0.2 μm for any subject, indicative of some upper sensor range rather than a subject trend.

The double-pass ocular point spread function was stored to verify that the correction achieved was tangible in all cases. For comparison, the open-loop point spread function was recorded as the average of 10 frames (typical exposure time 0.3 s) with the Badal at zero and the DM at bias position. For the closed-loop data, the DM was frozen at the correcting voltages immediately after a scan. The subjects were asked not to blink during acquisition. The plane of best focus for the open-loop measurements was determined subjectively by translating the science camera manually along the optical axis to find the sharpest image for each subject. This process was repeated prior to recording of the closed-loop point spread function to take account of any focus change due to the Badal setting or DM shape. Open- and closed-loop point spread functions for a few subjects are shown in Fig. 8 to illustrate the change that occurs with AO. Note that the point spread function recorded for subject 6 is almost diffraction limited, even without any correction. This was also true for subject 5 who had naturally low aberrations. For all other subjects, the extent of the point spread function was reduced with AO correction.

Some extra closed-loop measurements were acquired for some subjects. With subject 5, we performed closed-loop correction at M5 but at three sampling options B8, B4, and B2 (equivalent to spatial sampling of 12, 24, and 48 points across the pupil diameter and temporal sampling of 83, 63, and 46 fps, respectively). This allowed us to check if the resolution of the measured gradient maps or the temporal sampling had any effect on AO performance. We found that it did not. This indicates that it was our DM actuator layout or resolution that limited the quality of correction in this work, not the wavefront sampling. With subject 8, we investigated the effect of varying the loop gain on closed-loop performance at B8M5. There was only a marginal difference between the final RMS values obtained for $g = 0.3$, 0.5 and 0.7 (0.038, 0.032, and 0.034 μm, respectively), indicating a good stability range for our system. With subject 6, we looked at the effect of different steering mirror modulations on closed-loop performance. We found that the final corrected RMS rose steadily as the modulation was increased—from 0.043 μm at M5 to 0.137 μm at M20, although in all cases this did represent good

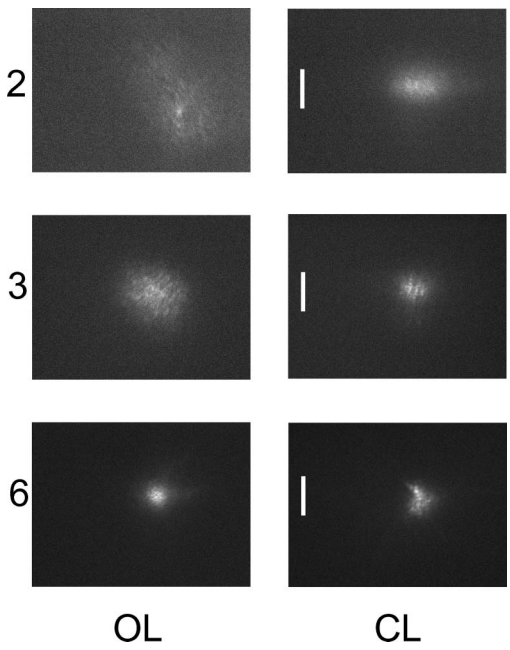

Fig. 8. Open-loop (OL) and closed-loop (CL) double-pass ocular point spread functions for subjects 2, 3, and 6. The probe beam width at the retina was 16 μm under diffraction-limited conditions. Magnification to the science camera was 24×. The white scale bar is equivalent to 50 μm on the retina.

correction when compared to the initial value of RMS just before loop closure.

D. Spectral Analysis

A spectral analysis of the time-varying RMS error was performed for each subject. Blinks were removed from the data prior to analysis by manually excluding certain time periods from the RMS trace. For closed-loop traces, we also excluded the time period before loop closure. The analysis was based on the Lomb–Scargle periodogram for nonuniformly spaced data [28]. Figure 9 shows the RMS error power spectra in open and closed loop, averaged in each case over all subjects. In the frequency range 2–20 Hz, a linear fit to each curve yields slopes of −1.9 and −2 for open and closed loop, respectively. We expect that the open-loop power spectrum should be approximately a straight line of slope ~ -1.5 for most subjects when focused at infinity [29]. Note that the open- and closed-loop results were obtained using different steering mirror modulation settings—M5 for closed loop and M20 for open loop. We did confirm that the power spectrum from an artificial eye was essentially flat with frequency at each modulation setting, and had very low magnitude compared to the spectrum from a real eye at the same modulation. This confirms that the power measured in the curves of Fig. 9 was due to the eyes dynamic aberrations. We also confirmed that the noise floor, represented by the power spectrum obtained from an artificial eye, did rise with modulation, being approximately 1 order of magnitude higher for M20 than for M5. These artificial eye power spectra at B8M5 and B8M20 are included in Fig. 9 to show the level of the noise floor at each setting. We noted that, apart from the noise floor at higher frequencies (≥10 Hz), the open-loop power spectra for subject 6 were identical at M5, M10, M15, and M20, providing further evidence that this subject's aberrations were sufficiently small is that they never saturated the pyramid wavefront sensor. Virtually all AO systems used to correct ocular aberrations are based on the Shack–Hartmann sensor. The usual way to estimate the bandwidth of such a system is to look at the ratio of closed-loop to open-loop power as a function of frequency—the so called disturbance power rejection curve [30]. The frequency where this curve crosses 1 for the first time is usually taken as a measure of system bandwidth. Clearly, we cannot use this criterion to estimate bandwidth here.

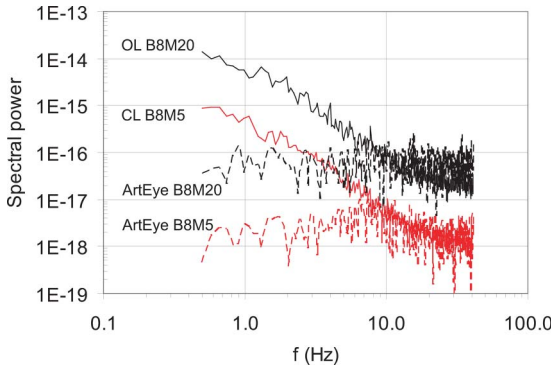

Fig. 9. (Color online) Solid lines: spectral power averaged over all subjects in open and closed loop. The open-loop data were recorded at B8M20, the closed-loop data at B8M5. Dashed lines: power spectra obtained from an artificial eye under the same conditions. The displacement of the noise floor with steering mirror modulation is clear for both artificial and real eyes. Note the small rise in power (5–10 Hz) in the artificial eye CL spectrum at B8M5—possibly associated with the rise in power expected at frequencies greater than the closed-loop bandwidth as discussed in the text?

5. Conclusion

We have presented well-calibrated open-loop measurements and adaptive correction of the aberrations of real eyes at 83 fps. We achieved correction down to our estimate of the wavefront reconstruction error (0.030 μm; see Fig. 3) for some subjects. We have demonstrated that, with the pyramid wavefront sensor, it is crucial that the experimental settings are chosen carefully for the task at hand. Open-loop operation requires good sampling (B4 rather than B8 in this work) and sufficient linear range for accurate measurements; the range required being subject dependent. In general, the best sensor range to use in open loop is not the one that will also optimize closed-loop performance unless the subject has very low aberrations; in that case, the benefit of doing AO at all is questionable. Once the loop is partially closed and the raw sensor signals approach zero, this task will always require small sensor range for maximum sensitivity for all subjects (M5 in this work). The required spatial sampling in closed loop is determined entirely by the resolution of the correcting device (B8 with our DM), although changing this does also impact loop speed. Given the opposing requirements of open- and closed-loop operation, it was not possible to estimate the bandwidth of our closed-loop system in the usual fashion. We did, however, confirm that the correction measured was real as evidenced by an improvement in the quality of the double-pass ocular point spread function for all subjects, apart from the two who were almost diffraction limited without correction. We conclude that the pyramid wavefront sensor is extremely versatile, but careful consideration must be given to the significance of each setting/choice when performing a particular task.

This work is supported by SFI grant number SFI/07/IN.1/1906. We are very grateful to Larry Thibos who provided us with his MATLAB files containing ocular aberration statistics and the functions to randomly generate the wavefronts of standard eyes. We are also very grateful to Salvador Bará who kindly gave us some phase plates allowing additional calibration of our system, and to Conor Leahy of the Applied Optics group for supplying the Matlab code for spectral analysis of the data.

References

1. J. Liang, D. R. Williams, and D. T. Miller, "Supernormal vision and high-resolution retinal imaging through adaptive optics," J. Opt. Soc. Am. A **14**, 2884–2892 (1997).
2. A. Roorda, F. Romero-Borja, W. J. Donnelly III, H. Queener, T. J. Hebert, and M. C. W. Campbell, "Adaptive optics scanning laser ophthalmoscopy," Opt. Express **10**, 405–412 (2002).
3. B. Hermann, E. J. Fernández, A. Unterhuber, H. Sattmann, A. F. Fercher, W. Drexler, P. M. Prieto, and P. Artal, "Adaptive-optics ultrahigh-resolution optical coherence tomography," Opt. Lett. **29**, 2142–2144 (2004).
4. B. Platt and R. V. Shack, "Lenticular Hartmann screen," Opt. Sci. Center Newsl. (University of Arizona) **5**, 15–16 (1994).
5. J. Liang, B. Grimm, S. Goelz, and J. Bille, "Objective measurement of wave aberrations of the human eye with the use of a Hartmann-Shack wave-front sensor," J. Opt. Soc. Am. A **11**, 1949–1957 (1994).
6. R. Ragazzoni, "Pupil plane wavefront sensing with an oscillating prism," J. Mod. Opt. **43**, 289–293 (1996).
7. A. Ghedina, M. Cecconi, R. Ragazzoni, J. Farinato, A. Baruffolo, G. Crimi, E. Diolaiti, S. Esposito, L. Fini, M. Ghigo, E. Marchetti, T. Niero, and A. Puglisi, "On sky test of the pyramid wavefront sensor," Proc. SPIE **4839**, 869–877 (2003).
8. L. M. Foucault, "Mémoire sur la construction des télescopes en verre arganté," Ann. Obs. Imp. Paris **5**, 197–237 (1859).
9. R. Ragazzoni, E. Diolaiti, and E. Vernet, "A pyramid wavefront sensor with no dynamic modulation," Opt. Commun. **208**, 51–60 (2002).
10. J. LeDue, L. Jolissaint, J.-P. Véran, and C. Bradley, "Calibration and testing with real turbulence of a pyramid sensor employing static modulation," Opt. Express **17**, 7186–7195 (2009).
11. I. Iglesias, R. Ragazzoni, Y. Julien, and P. Artal, "Extended source pyramid wave-front sensor for the human eye," Opt. Express **10**, 419–428 (2002).
12. J. B. Costa, R. Ragazzoni, A. Ghedina, M. Carbillet, C. Verinaud, M. Feldy, S. Esposito, E. Puga, and J. Farinato, "Is there need of any modulation in the pyramid wavefront sensor," Proc. SPIE **4839**, 288–298 (2003).
13. S. R. Chamot, C. Dainty, and S. Esposito, "Adaptive optics for ophthalmic applications using a pyramid wavefront sensor," Opt. Express **14**, 518–526 (2006).
14. R. Ragazzoni and J. Farinato, "Sensitivity of a pyramidic wave front sensor in closed loop adaptive optics," Astron. Astrophys. **350**, L23–L26 (1999).
15. S. Esposito and A. Riccardi, "Pyramid wavefront sensor behaviour in partial correction adaptive optic systems," Astron. Astrophys. **369**, L9–L12 (2001).
16. A. Riccardi, N. Bindi, R. Ragazzoni, S. Esposito, and P. Stefanini, "Laboratory characterization of a "Foucault-like" wavefront sensor for adaptive optics," Proc. SPIE **3353**, 941–951 (1998).
17. A. Burvall, E. Daly, S. R. Chamot, and C. Dainty, "Linearity of the pyramid wavefront sensor," Opt. Express **14**, 11925–11934 (2006).
18. N. Devaney, E. Dalimier, T. Farrell, D. Coburn, R. Mackey, D. Mackey, E. Daly, and C. Dainty, "The correction of ocular and atmospheric wavefronts: a comparison of the performance of various deformable mirrors," Appl. Opt. **47**, 6550–6561 (2008).
19. L. N. Thibos, A. Bradley, and X. Hong, "A statistical model of the aberration structure of normal, well-corrected eyes," Ophthalmic Physiolog. Opt. **22**, 427–433 (2002).
20. O. Feeney, "Theory and laboratory characterization of a novel wavefront sensor for adaptive optics," PhD thesis (National University of Ireland, Galway, 2001).
21. S. Esposito, O. Feeney, and A. Riccardi, "Laboratory test of a pyramid wavefront sensor," Proc. SPIE **4007**, 416–422 (2000).
22. R. Cubalchini, "Modal wave-front estimation from phase derivative measurements," J. Opt. Soc. Am. **69**, 972–977 (1979).
23. H. Hofer, L. Chen, G. Y. Yoon, B. Singer, Y. Yamauchi, and D. R. Williams, "Improvement in retinal image quality with dynamic correction of the eye's aberrations," Opt. Express **8**, 631–635 (2001).
24. P. Rodríguez, R. Navarro, J. Arines, and S. Bará, "A new calibration set of phase plates for ocular aberrometers," J. Refractive Surg. **22**, 275–284 (2006).
25. L. N. Thibos, R. A. Applegate, J. T. Schwiegerling, and R. Webb, "Standards for reporting the optical aberrations of eyes," in *Vision Science and Its Applications*, Vol. 35 of Trends in Optics and Photonics Series, V. Lakshminarayanan, ed. (Optical Society of America, 2000), pp. 233–244.
26. *British-Adopted European Standard BS EN 60825-1:2007 Safety of Laser Products- Part 1: Equipment Classification and Requirements* (British Standards Institution, 2009).
27. L. N. Thibos, X. Hong, A. Bradley, and X. Cheng, "Statistical variation of aberration structure and image quality in a normal population of healthy eyes," J. Opt. Soc. Am. A **19**, 2329–2348 (2002).
28. J. D. Scargle, "Studies in astronomical time series analysis. II. Statistical aspects of spectral analysis of unevenly spaced data," Astrophys. J. **263**, 835–853 (1982).
29. H. Hofer, P. Artal, B. Singer, J. L. Aragón, and D. R. Williams, "Dynamics of the eye's wave aberrations," J. Opt. Soc. Am. A **18**, 497–506 (2001).
30. K. M. Hampson, "Adaptive optics and vision," J. Mod. Opt. **55**, 3425–3467 (2008).